Fast In-Situ Triaxial Remanent Magnetic Field Measurement for Single-Beam SERF Atomic Magnetometer Based on Trisection Algorithm

Tengyue LONG[1], Bangcheng HAN[1,2], Xinda SONG[1,2*], Yuchen SUO[1], and Le JIA[1]

[1]*Department of Instrumentation Science and Opto-Electronics Engineering, Beihang University, Beijing 100191, China*

[2]*Hangzhou Extremely Weak Magnetic Field Major Science and Technology Infrastructure Research Institute, Hangzhou 310051, China*

[*]Corresponding author: Xinda SONG E-mail: songxinda@buaa.edu.cn1

Abstract: We demonstrate a method for quickly and automatically detecting all three components of a remanent magnetic field around a shielded spin-exchange relaxation-free (SERF) atomic magnetometer (AM) using the trisection algorithm (TSA) for zero-field resonance (ZFR). To satisfy the measurement of AMs, a resonance light of the ^{87}Rb D1 line with a spectral width of less than 1 MHz is converted to circular polarization by a linear polarizer and a quarter-wave plate. After the light beam has passed through the alkali metal vapor cell, the residual magnetic field can be measured by searching for triaxial ZFR optical peaks. The TSA stably reduces the measurement time to 2.41 s on average and improves the measurement accuracy, significantly outpacing existing methods. The weighted averages of all measurements with corresponding uncertainties are (–15.437 ± 0.022) nT, (6.062 ± 0.021) nT, and (–14.158 ± 0.052) nT on the *x*-, *y*-, and *z*-axes, respectively. These improvements could facilitate more extremely weak magnetic studies in real time, such as magnetoencephalography (MEG) and magnetocardiography (MCG) measurements.

Keywords: Atomic magnetometer; remanent magnetic field measurement; spin-exchange relaxation free; trisection algorithm

Citation: Tengyue LONG, Bangcheng HAN, Xinda SONG, Yuchen SUO, and Le JIA, "Fast In-Situ Triaxial Remanent Magnetic Field Measurement for Single-Beam SERF Atomic Magnetometer Based on Trisection Algorithm," *Photonic Sensors*, 2023, 13(3): 230311.

1. Introduction

High-sensitivity magnetic field measurement plays a significant role in fields ranging from physics to medicine [1–5]. Owing to their exceptional advantages, such as the high sensitivity of about 1 fT/Hz$^{1/2}$ and wide bandwidth of over 1 MHz, low-temperature superconducting quantum interference devices (SQUIDs) have historically been at the forefront of the field of ultrasensitive magnetic field measurements for nearly half a century [6–8]. Although the SQUID technology has reached a sufficient level of maturity and SQUID-based magnetometers are already commercially available, the necessary cryogenics and the ongoing need for costly liquid helium raise their running costs [9, 10]. Moreover, the sensor cannot be placed close to the source signal being tested due to the required thermal insulation, which would lower the measurement accuracy. In the last 20 years, the sensitivity of atomic magnetometers (AMs) based on the interaction of resonant

Received: 26 October 2022 / Revised: 23 January 2023
© The Author(s) 2023. This article is published with open access at Springerlink.com
DOI: 10.1007/s13320-023-0684-y
Article type: Regular

magneto-optics with atomic vapor has rivaled and even surpassed some cutting-edge SQUIDs [11–13]. AMs are viewed as a promising alternative to SQUIDs due to their inherent benefits of not requiring cryogenic cooling and permitting closer proximity to the magnetic source. Currently, AMs have considerable promise for use in many fields, including fundamental physics research [14–17], geophysical and deep-space exploration [2, 18, 19], portable magnetoencephalography (MEG) [20–23], and magnetocardiography devices (MCG) [24–27].

The majority of contemporary AMs typically employ polarized alkali metal vapor as their sensor medium, and spin-exchange collisions between the alkali atoms serve to constrain the transverse spin relaxation time. The spin-exchange relaxation-free (SERF) regime was first achieved by Happer *et al*. [28]. AM's exceptional sensitivity of 0.16 $fT/Hz^{1/2}$ has been demonstrated in Romalis's laboratory [29, 30]. Typically, there are two general approaches to reaching the SERF regime. One is to increase the temperature and alkali metal density to a particular magnetic field range to increase the spin exchange rate [31]. The alternative is to lower the residual magnetic field to a specific operating temperature range to lower the Larmor precession rate [32]. The need for an operating temperature can be reduced if the remanence around the AM is monitored correctly and corrected.

The traditional techniques of measuring the residual magnetic field along three axes require positioning a magnetic field sensor near a sensitive unit based on the SERF regime, gathering field data, and correcting the fields using three-axis Helmholtz or bi-planar coils [33–36]. Although these technologies handle a wide range of corrective effects, they are likely to generate mutual interference among the numerous sensors found within magnetic shielding. Furthermore, when measuring extremely weak magnetic fields, the gradient field within the shielded environment may cause the field information collected by nearby sensors to differ from the remanent magnetic field around the SERF AM's sensitive unit, resulting in larger measurement errors [37]. To overcome this problem, an appropriate in-situ magnetic field correction approach is required.

To address in-situ magnetic field measurement with the SERF AM, Romalis *et al*. [38] first demonstrated the feasibility of a cross-modulation-based method for in-situ field measurement under unshielded conditions in 2004. However, this did not have a specific convergence condition. As such, it was difficult to measure magnetic fields accurately. To cover this gap, Li *et al*. [39] performed a *z*-axis parameter modulation approach for atomic magnetometers in shielded environments, adopting phase flip as its judgment condition, which improved the measurement accuracy. However, these approaches are only relevant to double-beam SERF atomic magnetometers and are unsuitable for downsizing to handle biomagnetic field measurements. Qin *et al*. [40] performed an in-situ field measurement method for the SERF atomic magnetometer using a single-beam configuration to address this gap. By solving Bloch's equation, they successfully established a relationship between magnetometer's output and polarization projection in the direction of pumped light. However, this can only be measured manually with the low accuracy. To solve this problem, Dong *et al*. [41] first proposed a stepwise convergence method for remanent magnetization measurement within 23 s. Their method significantly improved the measurement accuracy and efficiency. Despite this, the process still has to be shortened since extended measurement durations might cause certain crucial magnetic field signals to be missed in real time. Besides, the measurement results of previous methods have not been analyzed systematically. Here's where we come in: to address the rapid and automatic measurement of the in-situ magnetic field, which is backed by the history supplied in the aforementioned literature.

To fill the gap and resolve the research problem, this paper presents a fast and automatic in-situ magnetic field measurement method based on the trisection algorithm (TSA) for the single-beam configuration SERF AM. This method does not require additional field sensor measurements. The photocurrent signal is captured by a precision acquisition circuit, and the obtained photoelectric signal is examined by a microprocessor. Convex optimization is used for the quick interval convergence of the recorded magnetic field range, leading to a quick measurement of the residual magnetic field in three dimensions. The entire residual magnetic field measurement procedure is automated, with a speed of approximately 2.41 s and high stability. This strategy is anticipated to work well in MCG and MEG applications and other real-time measurement fields that need SERF AMs.

Section 2 of this paper introduces TSA's measurement principle of remanent magnetic fields and presents the theoretical and analytical methods. Section 3 presents a simulation analysis of the method. Section 4 designs relevant experiments to verify the method's feasibility, and Section 5 discusses the measured values and the associated uncertainty analysis. Finally, Section 6 concludes this paper.

2. Principles and methods

2.1 SERF AM and magnetic field measurement

The underlying principles of AMs are to measure the time evolution of atomic spin polarization created by optical pumping. The spin-exchange broadening is minimized when SERF AMs are operating in a low magnetic field with high alkali-metal density. In SERF regimes, the dynamics of electron spins in their ground state can be described by the Bloch equation shown in (1):

$$\frac{\mathrm{d}}{\mathrm{d}t}\mathbf{P}=\frac{1}{q(P)}\left[\gamma_e\mathbf{B}\times\mathbf{P}+\left(R_{\mathrm{op}}\cdot s\mathbf{z}-\mathbf{P}\right)-R_{\mathrm{rel}}\mathbf{P}\right] \quad (1)$$

where **P** is the vector of the atomic polarization rate, **B** is the vector of the applied magnetic field, s is the photon polarization of the pumping beam, $q(P)$ is the slowing down, $\gamma_e=2\pi\times28$ MHz/G is the electron gyromagnetic ratio, R_{op} is the optical pumping rate, R_{rel} is the sum of all depolarization rates apart from the optical pumping rate, and **z** is the direction of the pumping light.

The directions of the pumping light and detection are defined as **z**. When the magnetic field changes slowly enough, the steady-state solution of the triaxial magnetic field can be shown in (2) [42]:

$$\begin{aligned}
P_x &= P_0\frac{\left(R_{\mathrm{tot}}/\gamma_e\right)B_y+B_xB_z}{B_x^2+B_y^2+B_z^2+\left(R_{\mathrm{tot}}/\gamma_e\right)^2}\\
P_y &= P_0\frac{-\left(R_{\mathrm{tot}}/\gamma_e\right)B_x+B_yB_z}{B_x^2+B_y^2+B_z^2+\left(R_{\mathrm{tot}}/\gamma_e\right)^2}\\
P_z &= P_0\frac{B_z^2+\left(R_{\mathrm{tot}}/\gamma_e\right)^2}{B_x^2+B_y^2+B_z^2+\left(R_{\mathrm{tot}}/\gamma_e\right)^2}
\end{aligned} \quad (2)$$

where $P_0=R_{\mathrm{op}}/R_{\mathrm{tot}}$ is the equilibrium spin polarization; B_x, B_y, and B_z indicate the total magnetic fields along the x, y, and z axes, respectively; $R_{\mathrm{tot}}=(R_{\mathrm{op}}+R_{\mathrm{rel}})$ is the total relaxation rate; $R_{\mathrm{tot}}/\gamma_e$ is the half-width at half maximum (HWHM) of the magnetometer, which is ΔB. The steady-state solution of the Bloch equation reveals the mathematical relations between the triaxial magnetic field and P_z.

According to the steady-state solution of P_z, it can be concluded that the z-axis polarization rate reaches its maximum value when the external magnetic field cancels with the remanent magnetic field in the x and y axes. Moreover, the z-axis polarization rate achieves its lowest value when the external magnetic field cancels out with the remanent magnetic field in z-axis.

Thus, this method can be used to measure the residual magnetic field precisely. This phenomenon is called the zero-field resonance (ZFR) of the SERF atomic magnetometer. However, as the polarization rate is an unmeasurable physical quantity, it must be

translated into an electrical signal by the photoelectric detector (PD). The electrical signal captured by the PD can be roughly described in (3):

$$\mathrm{PD} \approx \mathrm{PD}_0\left(1-\mathrm{e}^{-\mathrm{OD}}\right)\cdot P_z + \mathrm{PD}_0\cdot \mathrm{e}^{-\mathrm{OD}} \tag{3}$$

where PD_0 is the output of the PD in the case of far detuning. OD is the optical depth, which can be described in (4):

$$\mathrm{OD} = nlr_e c f_{\mathrm{D1}} \frac{\Gamma_{\mathrm{D1}}/2}{\left(\nu_{\mathrm{pump}}-\nu_{\mathrm{D1}}\right)^2+\left(\Gamma_{\mathrm{D1}}/2\right)^2} \tag{4}$$

where n is the density of alkali metal atoms, l is the length of the atomic cell, r_e is the classical electronic radius, c is the speed of light in a vacuum, f_{D1} is the oscillation of D1 line intensity, Γ_{D1} is the pressure spreading value of D1 line, ν_{pump} is the frequency of pumping light, and ν_{D1} is the central frequency of the D1 line of alkali metal atoms.

The photoelectric signal contains information on the three-axis magnetic field. According to the characteristics of the steady-state solution, sweeping the field with a coil in each axis produces a forward Lorentzian curve along the sensitive axes (x and y) and a reverse Lorentzian curve in the drawing axis (z). When the magnetic field in one of the axis directions is zero, the magnetometer's reaction reaches its peak value. The process is shown in Fig. 1.

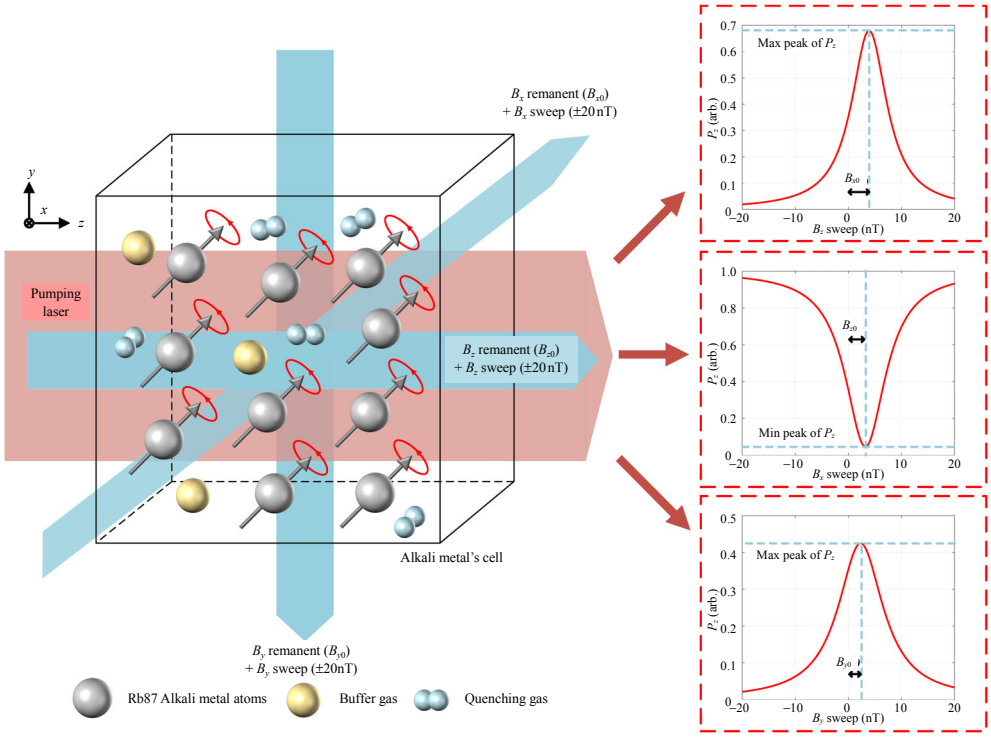

Fig. 1 Schematic of ZFR in the SEFR AM. In each of the three axes, a magnetic field sweeping ranging from –20 nT to 20 nT is applied. The response in the x- and y-axes is a forward Lorentzian line pattern, and the response in the z-axis is a reverse Lorentzian line pattern. The residual magnetic field is the magnitude of the magnetic field corresponding to the extreme point of the response along the three axes.

2.2 TSA for measurement

From Fig. 1, it can be seen that the in-situ magnetic field measurement of the SERF AM is completed based on the peak finding of the triaxial optical signal. Though the process has been automated, the speed still needs to be improved. If the measurement is inefficient, some weak magnetic signals with high timeliness may be missed. Moreover, none of the past methods had a systematic analysis of measurement results.

Therefore, this paper proposes a fast automatic in-situ magnetic measurement algorithm for a single-beam SERF AM based on the TSA. The

algorithm accomplishes the magnetic field measurement rapidly and accurately via the SERF AM in 2.4 s.

The TSA is a method for dealing with the problem of finding extreme values for single-peaked functions. Commonly used methods, such as the bisection method and Brent's method, are faster but more applicable to the problem of finding the zero of a function. According to the principle in Section 2.1, measuring residual magnetic fields involves finding extreme values. Therefore, the TSA and the similar golden section method are more suitable for solving the problem of magnetic field measurement. The basic principle of the TSA is to set the search-space number domain as U. A_1, A_2, and A_3 are the trisection intervals of U. The merged set of A_1, A_2, and A_3 is U, and the intersection of each other is the empty set. Let ξ be the boundary point between A_1 and A_2, and η be the boundary point between A_2 and A_3. The TSA updates and iterates the two-dimensional random variable $(\xi \text{ and } \eta)$ to change the trisection intervals, causing the tri-molecular domain interval distance to converge to the preset condition, ε. The magnetic field measurement is completed when the maximum value of the interval length of A_1, A_2, and A_3 is less than ε. The specific steps are described below, using the x-axis as an example:

Step 1: set the analytical formula of the Lorentzian curve function to $P(x)$. Select the two abscissae at the left and right ends of the Lorentzian curve away from the central point as the left endpoint of the tri-molecular domain A_1, named l, and the right endpoint of the tri-molecular domain A_3, named r, respectively, and obtain the function values, $P(l)$ and $P(r)$, corresponding to the Lorentzian curve.

Step 2: update the two-dimensional random variable by the iterative formula of the TSA. The iterative formula is shown in (5):

$$\begin{aligned} \xi &= l + \frac{1}{3}(r-l) \\ \eta &= l + \frac{2}{3}(r-l). \end{aligned} \tag{5}$$

Step 3: update the number field by comparing the size of the function values, $P(\xi)$ and $P(\eta)$, and prepare for the next iteration cycle update. If $P(\xi) \leqslant P(\eta)$, there must be no maximum value for the number field in the subdomain, A_1; thus, A_1 is discarded, and the number field, U, is updated again. At this time, U is the union of A_2 and A_3 from the previous iteration, and we re-divide the tri-molecular domains. The right endpoint, r, remains unchanged, and the left endpoint, l, is updated to ξ. Similarly, if $P(\xi) > P(\eta)$, we discard the subdomain, A_3, re-update the number domain, U, and re-divide the three-molecular domain. The right endpoint, r, is updated to η, and the left endpoint, l, remains unchanged. If the two values are equal, we select any step.

Step 4: determine whether the distance of the tri-molecular domain has entered the preset convergence condition, $|\xi - \eta| > \varepsilon$. If the convergence condition is met, exit the loop and complete the magnetic field measurement; otherwise, return to Step 2. The specific algorithm steps are shown in Table 1.

Table 1 TSA Algorithm.

Algorithm TSA

Input: interval: [l, r];objective function: $P(x)$; accuracy: ε; trisection points: ξ and η
Output: Peak value
while $|\xi - \eta| > \varepsilon$ **do**
$\xi = l + \frac{1}{3}(r-l)$; $\eta = l + \frac{2}{3}(r-l)$
if $P(\xi) \leqslant P(\eta)$; $l = \xi$;
else if $P(\xi) > P(\eta)$; $r = \eta$;
else $l = \xi$; $r = \eta$;
end while
Return peak value = $\frac{\xi + \eta}{2}$

A quantitative analysis of the TSA iterations is presented next. Note that one of the three

trimolecular domains of the TSA is discarded each round, and then, the third iteration is performed again. The problem can be transformed into the reduction of an interval [l, r]. First, the iterative TSA formula is described in (6):

$$(r_n - l_n) = \left(\frac{2}{3}\right)^n \cdot (r - l). \tag{6}$$

Thus, the number of iterations N_{TSA} can be obtained as a range of values in (7):

$$N_{\mathrm{TSA}} = \left[\frac{\ln\left(\frac{r-l}{\varepsilon}\right)}{\ln 3 - \ln 2}\right] + 1. \tag{7}$$

3. Simulation

To illustrate the efficacy of the TSA for the in-situ measurement of magnetic fields, we perform a simulation analysis.

First, we use ^{87}Rb atomic vapor, where $\gamma_e = 2\pi \times 28$ MHz/G is the gyromagnetic ratio of the bare electron, and we assume that the HWHM ΔB is 10 nT. As the remanent magnetic field in the magnetic shielding is less than 20 nT, we set the measurement range to ±20 nT for the simulation. The initial magnetic value search interval is set to [–20, 20] nT. The convergence condition of the TSA is set to $\varepsilon = 1$ pT, the system's maximum magnetic field compensation accuracy. Assuming that the magnitudes of magnetic fields in the x, y, and z axes are –3.5 nT, 2.5 nT, and 1.5 nT, respectively, the simulation results are shown in Fig. 2.

Figures 2(a), 2(b), and 2(c) represent the measurement process along the x, y, and z axes, respectively. The search period rapidly nears the remanent magnetization point. In Fig. 2(d), all three axes are set by our simulation. With our specified convergence conditions, all three axes converge 21 times, which is quick enough to receive exact results. It is worth noting that the number of convergences measured by the TSA is the same for all three axes, although the residual magnetic fields are set differently. This indicates the excellent stability of the convergence iteration process as applied by the TSA.

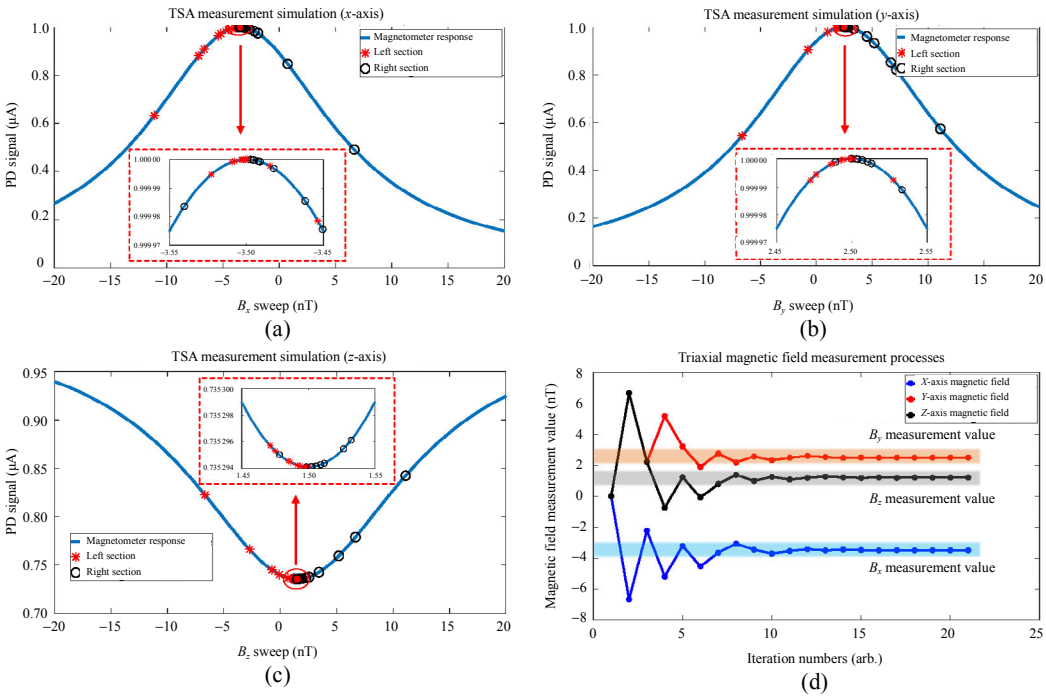

Fig. 2 Simulation of a three-axis magnetic field measurement process: (a), (b), and (c) correspond to the fast magnetic field convergence process in the x- (–3.5 nT), y- (2.5 nT), and z- (1.5 nT) axes under the TSA algorithm; (d) demonstrates the triaxial magnetic field measurement process. The number of iterations for all three axes is 21, indicating that the algorithm is more stable between different remanent magnetic fields.

4. Experiment

4.1 Experimental structures

The schematic and image of the experimental apparatus are shown in Fig. 3. A cubic cell made of borosilicate glass with an outer length of 4 mm and an inner length of 3 mm for the experiment. A little drop of 99.9% isotopically pure ^{87}Rb is placed into the glass cell after it is thoroughly evacuated, baked, and filled. Additionally, the cell contains 700 torr ^{4}He to prevent atom diffusion and 50 torr N_2 to extinguish the excited state. The vapor cell is housed in a thermally conductive boron-nitride ceramic oven, which is heated to 145 ℃ using a twisted-pair winding resistor powered by a 400 kHz alternating current (AC) signal. A real-time proportional-integral-derivative (PID) controller, along with a nonmagnetic Pt1000 temperature monitor, is employed to maintain temperature stability within a variation of less than 10 mK.

A polarization-maintaining fiber (PMF) is linked to a tunable distributed feedback (DFB) laser that emits the resonance light of the ^{87}Rb D1 line with a spectral width of less than 1 MHz. A 2.7 mm Gaussian beam is created by a series of collimating lenses. The pumping beam is then polarized circularly using a quarter-wave plate and a linear polarizer. To increase the amount of light that interacts with the alkali metal, the pump beam is pointed through the center of the cell. A PD then detects the transmitted beam. We build a circuit system to collect PD signals with the trans-impedance amplifier modules and transfer them by the analog-to-digital converter (ADC) through the single end to differential modules. The control signal generated by the personal computer (PC) is then transmitted to the digital-to-analog converter (DAC) and voltage-controlled current source modules. The current measures the AM's remnant magnetic field with its measurement coils.

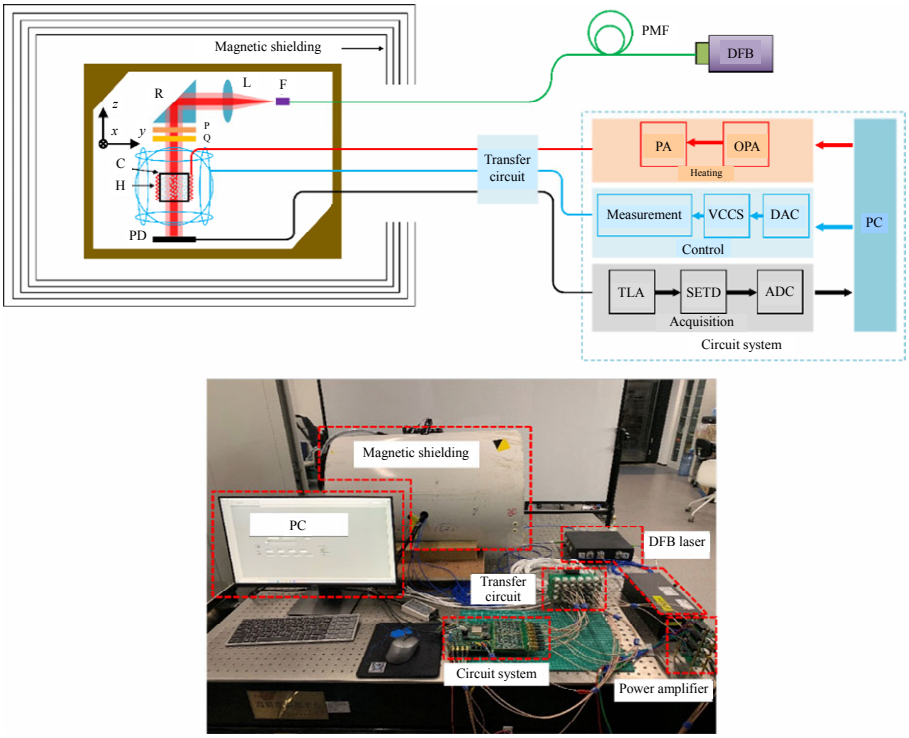

Fig. 3 Experimental diagram and actual photographs: (a) measurement experimental block diagram (the AM is in the magnetic shielding. H: heat coils; C: rubidium vapor cell; Q: quarter wave plate; P: linear polarizer; R: reflecting prism; L: collimating lens; F: fiber port; PA: power amplifier; OPA: operational amplifier; VCCS: voltage-controlled current source; TIA: trans-impedance amplifier; SETD: single-ended to differential, a circuit structure for use with a fully differential high-precision ADC) and (b) sensor performance testing platform.

4.2 Experimental configurations and steps

The measurement steps of the TSA are as follows:

Step 1: place the single-beam SERF AM into the magnetic shielding, which consists of one layer of aluminum and three layers of permalloy, and attenuate the ambient magnetic field by a quasi-static factor of approximately 10^5.

Step 2: begin the measurement after initializing the platform. First, set the initial search interval for the three-axis magnetic field. As the residual magnetic in the magnetic shielding is less than 20 nT per the calibration, the minimum value of the search interval is –20 nT, and the maximum is 20 nT. The search range is changed for the better analysis of the measurement results, and the resulting uncertainty analysis is given next.

Step 3: obtain the corresponding two-dimensional random variable (ξ and η) from the initial value through the TSA, as described in Step 2, via the high-precision and low-noise DAC output of two control signals corresponding to the two-dimensional random variable value of the x-axis. After each output, the output signal of the high-precision ADC is collected separately, and the two signals are compared. The search interval is reduced by the principle described in Step 2.

Step 4: when the norm of the two-dimensional random variable interval reaches the predetermined convergence value, seeking-interval updates are stopped. Then, the central value of the two-dimensional random variable interval is the measurement result of the x-axis remanence acquired by the TSA. Then, we continue to use the TSA to measure the y and z axes, where we find the minimum value of the z-axis. If the norm does not reach the predetermined convergence value, return to Step 3.

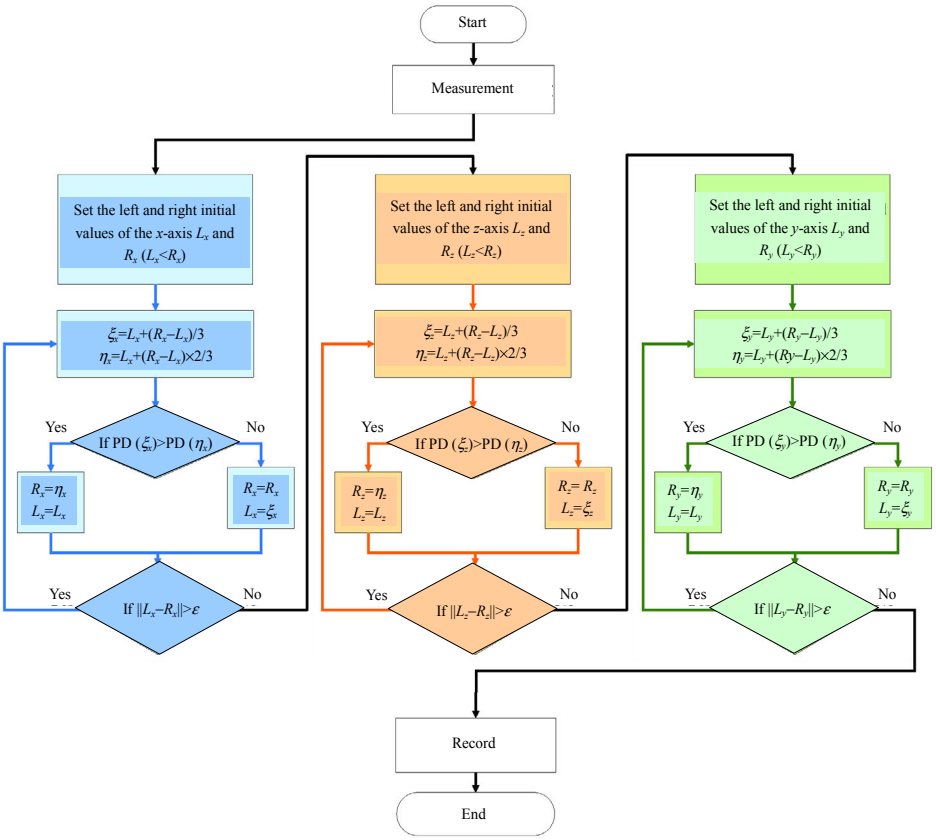

Fig. 4 Flow diagram of the residual magnetic field measurement using the TSA in the SERF magnetometer.

The above experiment is repeated ten times, and the average of the measurements is taken. Next, the initial interval of the experiment is reduced by 0.5 nT from both ends, i.e., [–19.5 nT, 19.5 nT], and the experiment is repeated ten times, and the average value is taken. The initial interval is then reduced by 0.5 nT and repeated to [–17 nT, 17 nT] for a total of seventy sets of experiments. Figure 4 illustrates the flow chart of one residual magnetic measurement.

5. Results and discussion

Figure 5 shows the total triaxial magnetic fields. The residual magnetic field should not depend on variations in the initial magnetic field. Here, we select the initial values, which increase from ±17 nT to ±20 nT in 0.5 nT intervals along the x, y, and z axes. The measurement results show that the magnetic fields along the axes are –15.437 nT, –14.158 nT, and 6.062 nT, respectively.

Here, we analyze the types A and B evaluations of measurement uncertainty [43], which are reflected by the error bars shown in Fig. 5. Unlike common measurement methods, the TSA does not have a formula for precise measurement. Thus, we begin by analyzing the type A evaluation of measurement uncertainty. The calculation formula is shown in (8):

$$u_a = \sqrt{\frac{1}{n(n-1)}\sum_{j=1}^{n}\left(x_j - \frac{1}{m}\sum_{i=1}^{m}x_i\right)^2} \tag{8}$$

where n = 7 is the number of measurement groups, and m = 10 is the number of measurements in each group in this paper. x_j is the triaxial magnetic field value measured by the TSA. According to the data, the values of u_a of the three axes are ± 0.0214 nT, ± 0.0201 nT, and ± 0.0518 nT, respectively.

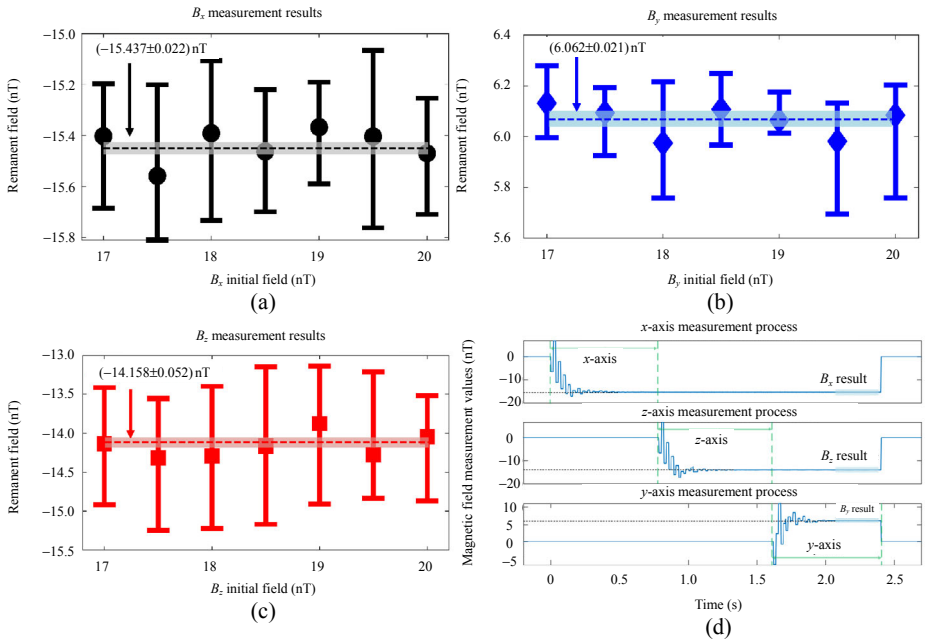

Fig. 5 Experimental values of triaxial residual field components with related estimated uncertainties by the TSA algorithm: (a), (b), and (c) demonstrate the triaxial residual field components, respectively (the weighted averages of global data points in the x, y, and z axes are –15.437 nT, 6.062 nT, and –14.158 nT, with the corresponding uncertainties shown by the hatched region, respectively), and (d) indicates the convergence process of the experimental triaxial magnetic field measurement in the range of [–20 nT, 20 nT].

Next, we solve the type B evaluations of the measurement uncertainty. As the ADC used in the measurement process is 16 bit, the reference voltage is 3 V, and the voltage in series with the triaxial coil is 1.8 kΩ, the instrumental uncertainty of the current is 0.025 mA. The coil constants of the triaxial magnetic coils in the SERF AM are 230.21 nT/mA, 261.33 nT/mA, and 253.47 nT/mA, and the distribution type of the measurement data can be approximated as a uniform distribution. Thus,

the inclusion factor, $k_b=\sqrt{3}$. The calculation formula is shown in (9):

$$u_b=\frac{\Delta_{\text{instrument}}C_{\text{coil}}}{k_b} \tag{9}$$

where $\Delta_{\text{instrument}}$ is the instrumental uncertainty, C_{coil} is the coil constants of the magnetic coils, and k_b is the inclusion factor of the type B evaluations of the measurement uncertainty. According to the data, u_b for the three axes is ± 0.003 4 nT, ± 0.0038 nT, and ± 0.0037 nT, respectively.

Finally, the types A and B standard uncertainties are used to estimate the combined standard uncertainty, u_c, which is calculated in (10):

$$u_c=\sqrt{u_a^2+u_b^2}\ . \tag{10}$$

Therefore, the weighted averages of magnetic data with the estimated uncertainties in the three axes are (–15.437 ± 0.022)nT, (6.062 ± 0.021)nT, and (–14.158 ± 0.052) nT, respectively.

Then, the measurement speed of the TSA and its stability are experimentally verified. The TSA could measure the three-axis magnetic field rapidly and complete the process in an average time of 2.41 s. In Fig. 5(d), a demonstration of the measurement process in one measurement range of ±20 nT is shown by an oscilloscope for the three axes, with the measurement sequence *x-z-y* (in line with the flow chart shown in Fig. 4). To facilitate the measurement time, we actively evacuate the magnetic field of the three axes after the measurement is completed, such that the time point at which the measurement ends can be determined by the inflection point. As seen in Fig. 6, the measurement time is about 2.4 s, and the time spent on all three axes is the same.

Moreover, the time variance of the TSA is extremely small, which greatly reduces variations over time (i.e., the measurement time is not affected by fluctuations in the ambient magnetic field). We perform 70 experiments with the initial magnetic field search interval ranging from ±20 nT to ±17 nT and record the times required for measurement, as shown in Fig. 6. The average measurement time is approximately 2.41 s, and its standard deviation is 0.033 s. To demonstrate the superiority of the TSA, we use the same experimental conditions for the measurements by using the traditional algorithm under the condition of its optimal parameters. As can be seen in Fig. 6, the average time taken by the traditional algorithm is 9.85 s, which is slower compared with the TSA. In addition, to demonstrate the accuracy of the TSA measurements, we use the measurements of both algorithms as the magnetic field compensation values of the SERF AM, apply a calibrated magnetic field signal of 100 pT_{rms} in 30 Hz, and measure the measurement sensitivity of the AM, as shown in Fig. 7. As can be seen from the figure, the measurement sensitivity under the TSA result reaches 26 $\text{fT/Hz}^{1/2}$, while the sensitivity under the traditional algorithm is 38 $\text{fT/Hz}^{1/2}$. Therefore, it can be seen that the measurement results under the TSA algorithm are more accurate than the traditional algorithm.

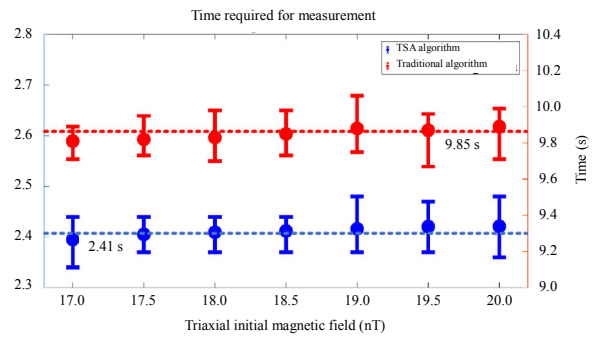

Fig. 6 Mean and error bands of the measurement times corresponding to the different measurement intervals. As can be seen from the figure, the average measurement time is around 2.41 s, which is faster than 9.85 s measured by the traditional algorithm.

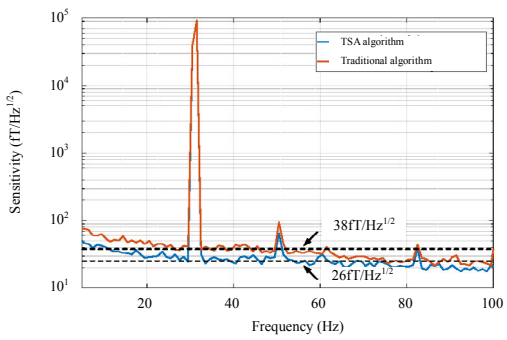

Fig. 7 Using the measured value as the compensation value, the measurement sensitivity of TSA is 26 $\text{fT/Hz}^{1/2}$, which is superior compared with the 38 $\text{fT/Hz}^{1/2}$ of the conventional algorithm.

6. Conclusions

In this paper, we demonstrate a fast in-situ triaxial remanent magnetic field measurement algorithm that intends to detect all three components of the residual magnetic field inside magnetic shielding by the SERF AM within a short time. For the first time, the residual magnetic field measurement problem is solved by using one of the optimal solution methods, the TSA, which provides a new idea for future magnetic field measurement research. Compared with the previous methods, the measurement speed and accuracy have been improved. The TSA enables measurement processes to be completed in approximately 2.41 s without the use of additional external sensors and devices. This achievement will be helpful to suppress the spin-exchange relaxation rate and capture a weaker magnetic signal in real time. There is a significant potential for future multichannel, real-time MCG and MEG measurements, and other applications of multiplexed and extremely weak magnetic field detection.

Acknowledgment

The authors would like to thank Jianzhi YANG for his help with this article.

This work was supported by Beijing Natural Science Foundation (Grant No. 4191002), Key Research & Development Program of Zhejiang, China (Grant No. 2020C01037), the National Key Research & Development Program of China (Grant No. 2018YFB2002405), and the National Natural Science Foundation of China (Grant No. 62073014).

Open Access This article is distributed under the terms of the Creative Commons Attribution 4.0 International License (http://creativecommons.org/licenses/by/4.0/), which permits unrestricted use, distribution, and reproduction in any medium, provided you give appropriate credit to the original author(s) and the source, provide a link to the Creative Commons license, and indicate if changes were made.

References

[1] Y. J. Kim, P. H. Chu, I. Savukov, and S. Newman, "Experimental limit on an exotic parity-odd spin-and velocity-dependent interaction using an optically polarized vapor," *Nature Communications*, 2019, 10(1): 1–7.

[2] M. Jiang, H. Su, A. Garcon, X. Peng, and D. Budker, "Search for axion-like dark matter with spin-based amplifiers," *Nature Physics*, 2021, 17(12): 1402–1407.

[3] H. Su, Y. Wang, M. Jiang, W. Ji, P. Fadeev, D. Hu, *et al.*, "Search for exotic spin-dependent interactions with a spin-based amplifier," *Science Advances*, 2021, 7(47): eabi9535.

[4] B. Dunkley, L. Da Costa, A. Bethune, R. Jetly, E. Pang, M. Taylor, *et al.*, "Low-frequency connectivity is associated with mild traumatic brain injury," *NeuroImage*, 2015, 7: 611–621.

[5] R. M. Hill, E. Boto, M. Rea, N. Holmes, J. Leggett, L. A. Coles, *et al.,* "Multi-channel whole-head OPM-MEG: Helmet design and a comparison with a conventional system," *NeuroImage*, 2020, 219: 116995.

[6] R. L. Fagaly, "Superconducting quantum interference device instruments and applications," *Review of Scientific Instruments*, 2006, 77(10): 1–4.

[7] E. Trabaldo, C. Pfeiffer, E. Andersson, M. Chukharkin, R. Arpaia, D. Montemurro, *et al.,* "Squid magnetometer based on grooved dayem nanobridges and a flux transformer," *IEEE Transactions on Applied Superconductivity*, 2020, 30(7): 1–4.

[8] J. Wu, X. Chen, Y. Yang, Q. Zhi, X. Wang, J. Zhang, *et al.*, "Application of tem based on HTS SQUID magnetometer in deep geological structure exploration in the Baiyun gold deposit, Ne China," *Journal of Earth Science*, 2021, 32(1): 1–7.

[9] A. Borna, J. Iivanainen, T. R. Carter, J. McKay, S. Taulu, J. Stephen, *et al.*, "Cross-axis projection error in optically pumped magnetometers and its implication for magnetoencephalography systems," *NeuroImage*, 2022, 247: 118818.

[10] S. Zou, H. Zhang, X. Y. Chen, and J. C. Fang, "In-situ triaxial residual magnetic field measurement based on optically-detected electron paramagnetic resonance of spin-polarized potassium," *Measurement*, 2022, 187: 110338.

[11] V. Lucivero, W. Lee, N. Dural, and M. Romalis, "Femtotesla direct magnetic gradiometer using a single multipass cell," *Physical Review Applied*, 2021, 15(1): 014004.

[12] C. Troullinou, R. Jiménez-Martínez, J. Kong, V. Lucivero, and M. Mitchell, "Squeezed-light enhancement and backaction evasion in a high sensitivity optically pumped magnetometer,"

Physical Review Letters, 2021, 127(19): 193601.

[13] J. Tang, Y. Zhai, L. Cao, Y. Zhang, L. Li, B. Zhao, *et al.*, "High-sensitivity operation of a single-beam atomic magnetometer for three-axis magnetic field measurement," *Optics Express*, 2021, 29(10): 15641–15652.

[14] M. Jiang, T. Wu, J. W. Blanchard, G. Feng, X. Peng, and D. Budker, "Experimental benchmarking of quantum control in zero-field nuclear magnetic resonance," *Science Advances*, 2018, 4(6): 6327.

[15] K. Wei, W. Ji, C. Fu, A. Wickenbrock, V. V. Flambaum, J. Fang, *et al.*, "Constraints on exotic spin-velocity-dependent interactions," *Nature Communications*, 2022, 13(1): 7387.

[16] M. Safronova, D. Budker, D. DeMille, D. F. J. Kimball, A. Derevianko, and C. W. Clark, "Search for new physics with atoms and molecules," *Reviews of Modern Physics*, 2018, 90(2): 025008.

[17] W. Ji, Y. Chen, C. Fu, M. Ding, J. Fang, Z. Xiao, *et al.*, "New experimental limits on exotic spin-spin-velocity-dependent interactions by using $SmCo_5$ spin sources," *Physical Review Letters*, 2018, 121(26): 261803.

[18] J. M. Higbie, S. M. Rochester, B. Patton, R. Holzlöhner, D. B. Calia, and D. Budker, "Magnetometry with mesospheric sodium," *Proceedings of the National Academy of Sciences*, 2011, 108(9): 3522–3525.

[19] M. E. Çetin, "Realtime magnetometer calibration for spinning aerospace vehicles," *Middle East Technical University*, 2022.

[20] E. Boto, N. Holmes, J. Leggett, G. Roberts, V. Shah, S. S. Meyer, *et al.*, "Moving magnetoencephalography towards real-world applications with a wearable system," *Nature*, 2018, 555(7698): 657–661.

[21] T. M. Tierney, N. Holmes, S. Mellor, J. D. L′opez, G. Roberts, R. M. Hill, *et al.*, "Optically pumped magnetometers: from quantum origins to multi-channel magnetoencephalography," *NeuroImage*, 2019, 199: 598–608.

[22] G. Zhang, S. Huang, F. Xu, Z. Hu, and Q. Lin, "Multi-channel spin exchange relaxation free magnetometer towards two-dimensional vector magnetoencephalography," *Optics Express*, 2019, 27(2): 597–607.

[23] R. Zhang, W. Xiao, Y. Ding, Y. Feng, X. Peng, L. Shen, *et al.*, "Recording brain activities in unshielded earth's field with optically pumped atomic magnetometers," *Science Advances*, 2020, 6(24): 8792.

[24] G. Bison, R. Wynands, and A. Weis, "Dynamical mapping of the human cardiomagnetic field with a room-temperature, laser-optical sensor," *Optics Express*, 2003, 11(8): 904–909.

[25] M. E. Pena, C. L. Pearson, M. P. Goulet, V. M. Kazan, A. L. DeRita, S. M. Szpunar, *et al.*, "A 90-second magnetocardiogram using a novel analysis system to assess for coronary artery stenosis in emergency department observation unit chest pain patients," *IJC Heart & Vasculature*, 2020, 26: 100466.

[26] S. Sengottuvel, S. S. Devi, M. Sasikala, S. Satheesh, and R. J. Selvaraj, "An epoch based methodology to denoise magnetocardiogram (MCG) signals and its application to measurements on subjects with implanted devices," *Biomedical Physics & Engineering Express*, 2021, 7(3): 035006.

[27] Y. Yang, M. Xu, A. Liang, Y. Yin, X. Ma, Y. Gao, *et al.*, "A new wearable multichannel magnetocardiogram system with a SERF atomic magnetometer array," *Scientific Reports*, 2021, 11(1): 1–11.

[28] W. Happer and H. Tang, "Spin-exchange shift and narrowing of magnetic resonance lines in optically pumped alkali vapors," *Physical Review Letters*, 1973, 31(5): 273.

[29] J. Allred, R. Lyman, T. Kornack, and M. V. Romalis, "High-sensitivity atomic magnetometer unaffected by spin-exchange relaxation," *Physical Review Letters*, 2002, 89(13): 130801.

[30] I. Kominis, T. Kornack, J. Allred, and M. V. Romalis, "A subfemtotesla multichannel atomic magnetometer," *Nature*, 2003, 422(6932): 596–599.

[31] S. Zhang, J. Lu, M. Ye, Y. Zhou, K. Yin, F. Lu, *et al.*, "Optimal operating temperature of miniaturized optically pumped magnetometers," *IEEE Transactions on Instrumentation and Measurement*, 2022, 71: 1–7.

[32] Z. Li, "Development of a parametrically modulated serf magnetometer," Ph.D. dissertation, The University of Wisconsin-Madison, 2006.

[33] J. Iivanainen, R. Zetter, M. Grön, K. Hakkarainen, and L. Parkkonen, "On-scalp MEG system utilizing an actively shielded array of optically-pumped magnetometers," *Neuroimage*, 2019, 194: 244–258.

[34] N. Holmes, J. Leggett, E. Boto, G. Roberts, R. M. Hill, T. M. Tierney, *et al.*, "A bi-planar coil system for nulling background magnetic fields in scalp mounted magnetoencephalography," *NeuroImage*, 2018, 181: 760–774.

[35] J. Wang, X. Song, W. Zhou, Y. Le, and X. Ning, "Hybrid optimal design of biplanar coils with uniform magnetic field or field gradient," *IEEE Transactions on Industrial Electronics*, 2020, 68(11): 11544–11553.

[36] Z. Ding, Z. Huang, M. Pang, and B. Han, "Iterative optimization algorithm to design bi-planar coils for dynamic magnetoencephalography," *IEEE Transactions on Industrial Electronics*, 2022, 70(2): 2085–2094.

[37] N. Holmes, T. M. Tierney, J. Leggett, E. Boto, S. Mellor, G. Roberts, *et al.*, "Balanced, bi-planar magnetic field and field gradient coils for field

compensation in wearable magnetoencephalography," *Scientific Reports*, 2019, 9(1): 1–15.

[38] S. Seltzer and M. Romalis, "Unshielded three-axis vector operation of a spin-exchange-relaxation-free atomic magnetometer," *Applied Physics Letters*, 2004, 85(20): 4804–4806.

[39] Z. Li, R. T. Wakai, and T. G. Walker, "Parametric modulation of an atomic magnetometer," *Applied Physics Letters*, 2006, 89(13): 134105.

[40] J. Fang and J. Qin, "In situ triaxial magnetic field compensation for the spin-exchange-relaxation-free atomic magnetometer," *Review of Scientific Instruments*, 2012, 83(10): 103104.

[41] H. Dong, H. Lin, and X. Tang, "Atomic-signal-based zero-field finding technique for unshielded atomic vector magnetometer," *IEEE Sensors Journal*, 2012, 13(1): 186–189.

[42] S. J. Seltzer, "Developments in alkali-metal atomic magnetometry," Ph.D. dissertation, Princeton University, 2008.

[43] E. Smith, "Uncertainty analysis," *Encyclopedia of Environmetrics*, 2002, 4: 2283–2297.